Tri-Band Dual-Polarized Shared-Aperture Antenna Arrays with Wide-Angle Scanning and Low Profile for 5G Base Stations

Sun, Ying; Zhang, Jin; Mei, Peng; Luo, Shengyuan; Fu, Wen; Zhang, Shuai

Published in:
I E E E Transactions on Antennas and Propagation

DOI (link to publication from Publisher):
10.1109/TAP.2024.3358611

Publication date:
2024

Document Version
Accepted author manuscript, peer reviewed version

Tri-Band Dual-Polarized Shared-Aperture Antenna Arrays with Wide-Angle Scanning and Low Profile for 5G Base Stations

Ying Sun, Jin Zhang, Peng Mei, *Member, IEEE,* Shengyuan Luo, Wen Fu, and Shuai Zhang, *Senior Member, IEEE*

***Abstract*—A novel tri-band shared aperture antenna (TSAA) array is proposed in this paper to meet the requirements of modern base station antennas for multi-band antenna fusion and independent control. Different antenna types are utilized for each operating band, including 3D-printed dielectric resonator antennas (DRAs) for the middle bands (MB, 3.4 to 3.6 GHz) and high bands (HB, 5.4 to 5.6 GHz), and dipole antennas for the low band (LB, 1.85 to 2.15 GHz). The TSAA comprises a 1x4 dipole antenna array for LB, a 2x7 MB antenna array located at the edges of the aperture, and a 2x12 HB antenna array at the aperture center. The LB dipole antenna array is positioned above the MB and HB antenna arrays, providing wideband electromagnetic transparency for both MB and HB simultaneously. By exploiting the high dielectric permittivity of the DRAs, the overall array profile is miniaturized to 0.13 λ_0 (λ_0 is the free-space wavelength at central frequency of LB), while the array element spacing meets scanning conditions for suppressing grating lobes and achieving wide-angle control of each frequency band. Additionally, the adoption of symmetric η-shaped stripline coupled feeding technology in the LB antenna effectively improves the problem of tilted radiation patterns of the HB antenna.**

***Index Terms*—Tri-band shared-aperture antenna array, frequency-selective surface (FSS), wide-angle scanning, 3D-printed dielectric resonator antenna, pattern restoration, low profile.**

I. Introduction

WITH the swiftly increasing demands of people for data transmission speed and data sending volume, more and more the fifth-generation (5G) communication system bands have been investigated for commercial applications around the world, for instance, 5.15 – 5.925 GHz in America, 3.3 – 3.6 and 4.8 – 5 GHz in China, 3.4 – 3.8 GHz in Europe, and 3.4 – 3.7 GHz in Korea [1]. Although 5G has been progressively used in various areas, it still requires to be compatible with its precursors, such as 4G, 3G, and even 2G systems for a pretty long period to support different communication protocols [2]. Even if antenna arrays designed in separate radiation apertures can satisfy these above-mentioned requirements, large sizes and weights are unavoidable in order to increase aperture utilization efficiency. To provide a large communication capacity within the very crowded and limited base station space, tri-band shared aperture antenna (TSAA) arrays, which integrate multiple antenna arrays in one single aperture, become one of the most promising solutions [3]–[7].

The authors are with the Antennas, Propagation and Millimeter-wave Systems (APMS) section, Department of Electronic Systems, Aalborg University, 9220 Aalborg, Denmark (e-mail: yisu@es.aau.dk; jzhang@es.aau.dk; mei@es.aau.dk; shengyuanl@es.aau.dk; wf@es.aau.dk; sz@es.aau.dk).

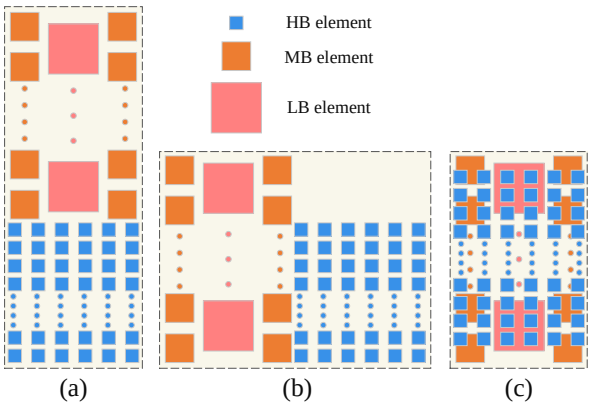

Fig. 1. Topological construction of the TSAA array. (a) Front-Back construction, (b) Left-Right construction, and (c) Fully-Shared construction.

Currently, plenty of research mainly focuses on low profile, mutual coupling suppression, and miniaturization of DSAA arrays. There are mainly two approaches to achieving a dual-band/multi-band base station antenna. One approach is to design an antenna that can operate at different bands [9]–[11]. However, when these antennas are designed to be arrayed, the spacing in the higher frequency band will be larger than one wavelength, leading to a significant increase in the grating lobe level. Another way is to pick separated antenna cells for each band, which must be placed ingeniously to avoid strong mutual coupling. The side-by-side [12]–[15], embedded [16]–[19] and top-bottom construction[2], [11], [20]–[23] are extensively applied in the development of dual-band/multi-band base stations with separated antenna cells.

For the side-by-side scheme, additional decoupling techniques such as filtering antennas are commonly needed to suppress mutual coupling [14], [15]. However, this method increases the overall construction width, which is contrary to the goal of compact design. Additionally, tilted radiation patterns will come out due to the asymmetrical array structure. The embedded construction method can solve the problem of asymmetric array structures, but the mutual coupling between each band must be carefully managed due to the more serious shielding effect [16], [17]. In the embedded construction method, the HB antenna element is placed inside the LB

antenna element with the physically larger radiation aperture without enlarging the overall size. However, a large frequency ratio is required to avoid the HB element being shielded by the LB element. The top-bottom construction method utilizes the radiator of the relatively larger LB antenna placed under the HB element as a reflector for the HB antenna. However, this method inevitably increases the antenna's height, which is not practical for applications.

To achieve a very low profile with a wide bandwidth in the antenna array, artificial magnetic conductors (AMCs) have been introduced [24]. However, a large ground plane is required to achieve 0° reflection phase in AMCs. In addition, the shielding effect of the LB element to the HB element needs to be eliminated, avoiding the scattering field of the LB antenna to distort the HB radiation pattern, which causes deflection of the main beam and gains reduction. Moreover, solutions for out-of-band scattering suppression, such as lumped inductors [25], [26] choke structures [27], and metasurface cloaks [28], were introduced to eliminate the shielding effect. Although the metasurface cloaks can restore distorted radiation patterns, they also introduce a large volume. Lumped inductors and choke structures are used to eliminate scattering to avoid additional size, but they inevitably affect the antenna's function.

Recently, the use of frequency-selective surface (FSS) for decoupling has been investigated [11], [19]. The LB element is introduced as an FSS with covering working band of the MB element. A two-layer FSS with periodic elements has been designed as the LB radiator in [19], which eliminates shielding to the MB element below. LB radiation and transmission can be separately controlled without affecting the LB antenna's performance. However, this approach mainly works on single-band decoupling. Although the dual-band decoupling has been proposed [11], the dual-band radiation of the wideband MB component is difficult to achieve the separate control of each band. The overall profile is limited by the dipole and patch antennas, resulting in a profile of nearly 0.25 λ_0 (λ_0 is the free-space wavelength at the central frequency of LB).

Nowadays, a few tri-band shared aperture antenna have been investigated. As shown in Fig. 1, there are three distributions for the TSAA array [8]: "Front-Back" topology, "Left-Right" topology, and "Fully-Shared" topology. They consist of dual-band shared aperture antenna (DSAA) arrays with an "edge to edge" arrangement and a massive multi-input-multi-output (MIMO) antenna array [8]. As depicted in Fig. 1(a) and 1(b), antenna arrays operating in different bands are placed side by side, which sharply increase the volume of the compound antenna array. Therefore, "Fully-Shared" topology is more suitable for the evolutionary trend of the base station antenna. However, the cross-band coupling interference will significantly increase due to the more compacted structure of "Fully-Shared" topology, which causes distortion in the radiation pattern, deterioration in port isolation, and input impedance mismatching.

As discussed, proposing a new array scheme with a low profile and applying novel antennas for multiband antenna arrays are essential to achieve a large scanning angle base station independently controlled for each band. In this article, A TSAA array is proposed with a deep "Fully-Shared" topology scheme, an LB antenna with a low profile and wideband FSS, and a DRA antenna to realize an overall low profile, miniaturization, high degree of freedom, and low coupling. To the authors' knowledge, this is the first proposal of a novel low-profile wide-angle scanning shared-aperture antenna array structure independently controlled in three frequency bands.

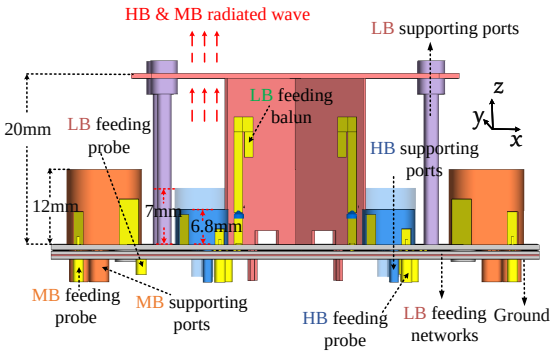

(a)

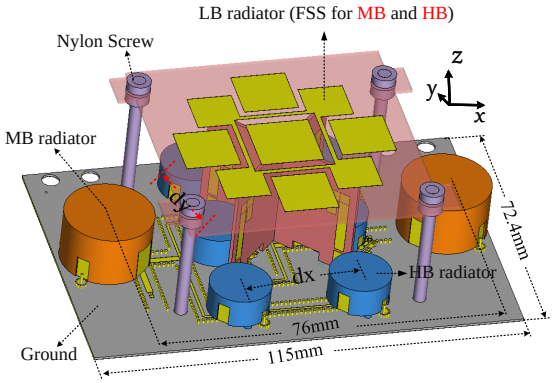

(b)

Fig. 2. Configuration of the sub-TSAA array. (a) Side view, and (b) Perspective view.

II. Sub-TSAA Construction and Working Mechanism of the Single Antenna Element

The construction of the proposed sub-TSAA array is presented in Fig. 2. Specifically, DRAs are employed for MB (3.4-3.6 GHz) and HB (5.4-5.6 GHz) antenna, while dipole antennas are utilized as LB (1.85-2.15 GHz) elements. The MB array comprises a 1 × 2 unit located at the edges of the aperture, and the HB array has a 2 × 3 unit positioned at the center of the aperture, as illustrated in Fig. 2(b). Additionally, the LB antenna is situated above the MB and HB antenna arrays, offering electromagnetic transparency for both MB and HB simultaneously. Notably, all antennas are uniformly distributed on the center axis or both sides of the reflector to ensure symmetrical far-field radiation patterns.

A multi-layer PCB (substrate1, substrate2, and substrate3) is used to design the feeding structure for different frequency bands in order to minimize the mutual coupling between the ports of different antennas. The bonding films Rogers 4450F, with a thickness of 0.202 mm, are utilized to bond the substrates together.

A. *A Single LB Antenna with Low Profile and Wideband FSS*

To ensure optimal array performance, the LB antenna must be electromagnetic (EM) transparent for both MB and HB radiation while maintaining the radiation performance. Even though the MB-DRAs are positioned on the border of the ground plane, which is not directly covered by the LB antenna, it is still essential to maintain EM transparency at MB to reduce blockages and reflections on the broadside direction, which could minimize distorted radiation and boost the gain. To thoroughly investigate the properties of the proposed low-profile FSS-based LB radiator, the wideband FSS is first analyzed, and subsequently, the differential-fed working mechanism with low Cross Polar Discrimination (XPD) is analyzed. All simulation results presented in this paper were obtained by using the commercial electromagnetic field simulation software, CST STUDIO SUITE (CST).

1) Construction of LB Antenna: The LB antenna configuration, consisting of a radiator with FSS, two baluns (Balun-1 and Balun-2) orthogonally arranged, and two differential feeding networks, is presented in Fig. 3. The radiator is comprised of a central squared patch, four same-sized squared patches on the four edges, and a loop positioned between these patches, all printed on the top layer of a Rogers RO4350B substrate (with ε_r = 3.66, δ = 0.0037, and thickness = 0.762 mm). The radiator's substrate also has four small holes on the corners to facilitate fixed nylon screws and prevent physical overlapping with the HB location.

Balun-1 and Balun-2 are fabricated on Rogers RO4350B substrates with a thickness of 0.762 mm and embedded orthogonally to each other for a robust structure. The four same-sized η-shaped striplines, printed on the baluns and connected to the differential feeding network are designed to ensure a low profile and low coupling with other bands for the entire structure. The feeding network consists of the stripline and isolation columns located in two layers of Rogers RO4350B substrates (substrate2 and substrate3), each with a thickness of 0.508 mm. The isolation columns help reduce crosstalk between balanced feeding networks, which can cause unwanted radiation and lower the antenna's efficiency.

2) Characteristics of the Proposed Wideband FSS: The FSS unit cell is simulated under the setup of periodic boundary along x- and y-axes, respectively. Two Floquet ports along the z-axis are employed to evaluate its transmission performance, and the period of the FSS is P= 72.4 mm, as shown in Fig. 4. Mode 1 and 2 represent the two polarization modes of ±45 degrees. The Model 1 is transparent and identical for both polarizations. Although the transmission coefficient and reflection coefficient show a sharp deterioration in the frequency band of 3.98-4 GHz, the required working frequency band for our design is not affected. For the frequency ranges of 3.4-3.6 GHz and 5.4-5.6 GHz, the insertion loss is less than 0.8 dB, as shown in the purple and pink area in Fig. 4 (a), covering the entire MB and HB. To achieve radiation characteristics based on Model 1 of Fig. 4 (a), a single loop is introduced to Model 1 to provide a current path, as depicted in Model 2 of Fig. 4 (b), primarily contributing to the radiation at LB. This combined patch is also transparent and identical for both polarizations at ±45 degrees, covering the entire MB and HB frequency ranges.

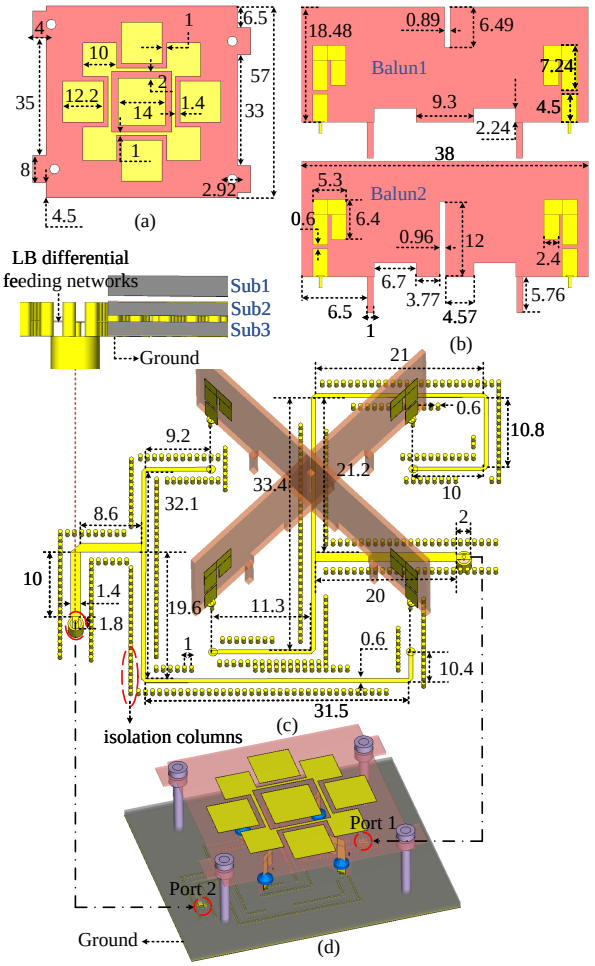

Fig. 3. Configuration of the proposed LB antenna element. (a) Top layer of radiator, (b) LB baluns, (c) perspective view of the proposed LB differential feeding networks, and (d) the 3-D view of a single LB antenna (Units: mm).

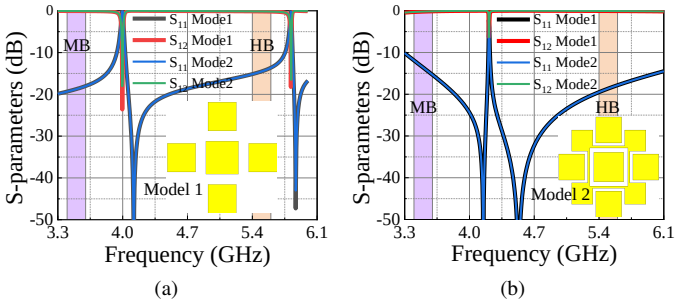

Fig. 4. S-parameters of with/without LB radiator in different modes. (a) Model 1 without radiator, and (b) Model 2 with radiator.

3) Differential Fed to Reduce Coupling of the Single Low-profile LB Antenna Element: As shown in Fig. 3(d), for the single LB antenna, the total profile is only 0.13λ_0 (λ_0 is the free-space wavelength at central frequency of LB). From our research, if the single LB antenna element proposed in this

paper is fed by the traditional method, the coupling of the LB antenna is too large to work normally. Consequently, the LB antenna is fed by capacitive coupling through four η-shaped striplines connected to a differential feeding network to excite the desired mode for broadside radiation.

Fig. 5 is used to illustrate the detailed working principle of the single LB antenna element by the current distribution, which only shows the scene when the port2 is excited due to a symmetrical patch shape and similar feeding structure. As shown in Fig. 5(a), the patches on the four corners of the square ring correspond to the port1+, port1-, port2+, and port2- respectively. When the same amplitude and 180-degree phase difference are used to excite port2+ and port2-, the currents on the radiation patch are synthesized into -45 degree polarization. As the black arrows show, the strong synthetic vector current on the middle ring is along the -45 degree direction and a -45 degree polarization is introduced and square patches corresponding to the port2+ and port2- also introduce -45 degree polarization to enhance the radiation. In addition, as yellow dashed arrows show, the currents around square patches corresponding to the port1+ and port1- form a loop and do not contribute to +45 degree polarization. Consequently, high XPD (Cross Polar Discrimination) at boresight is realized. In addition, the proposed antenna has high isolation in theory. It also can be illustrated by the current distribution of Fig. 5(a). Due to the coupled vector currents around two corners of the patch being strictly symmetrical to the centre of the ring patch, the voltage difference between port1+ and port1- is nearly zero. Therefore, the introduced currents cannot enter port 1, and high isolation is realized.

As a result, the radiator without FSS Model 1 can achieve both high XPD and high isolation in the case of the relatively low profile. Then, the FSS Model 1 previously mentioned is combined with this radiator to achieve transparency function to MB and HB antennas on the condition of low profile and low cross-polarization. Fig. 5 illustrates a comparison between the current distribution with and without the FSS Model 1 when port 2 is excited, indicating that the Model 1 did not significantly alter the original radiator's current distribution. The EM radiation mainly concentrates on the original radiator, as the light purple dashed lines in Fig. 5(b) show, despite Model 1 induced surface currents, these currents don't contribute to the -45° polarization due to looped currents induced on each square patch of Model 1. Fig. 6 shows a comparison of the electric field distribution at 2.15 GHz with and without Model 1 when port 2 is excited, demonstrating the very slight effect on the original antenna's radiation from the addition of Model 1.

Fig. 7 demonstrates the performance of the proposed LB dipole antenna of Fig. 3 (d). The HPBWs of the excited port2 with and without FSS Model 1, are shown in Fig. 7(a). It can be observed that the combined antenna with transparency function retains a stable HBPW in a low profile and there is insignificant impact on the HPBWs upon adding FSS Model 1. The impedance bandwidths (return loss > 10 dB) range from 2.08 to 2.2 GHz. At the operating frequency, the self-cross-polarization coupling is less than -30dB and a half-power beamwidth of approximately 90 degrees can be achieved.

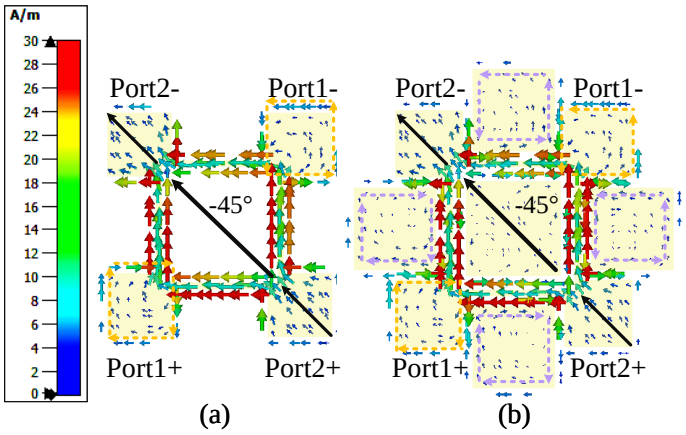

Fig. 5. Comparison of the current distributions on the LB antenna at 2.15 GHz. (a) Without proposed FSS Model 1, and (b) with proposed FSS Model 1.

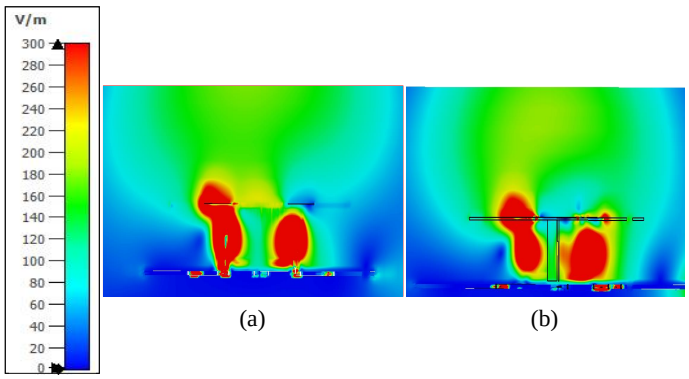

Fig. 6. Comparison of the E-field distributions on the LB antenna at 2.15 GHz. (a) Without proposed FSS Model 1, and (b) with proposed FSS Model 1.

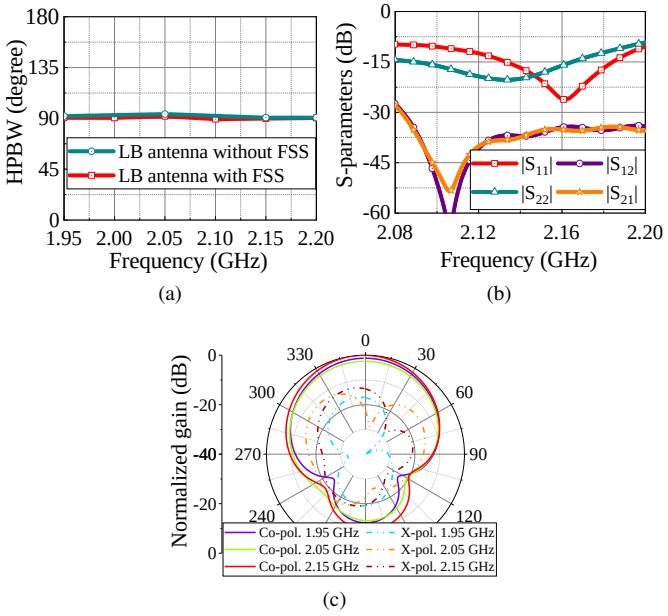

Fig. 7. Simulated horizontal HPBWs, S parameters, and radiation patterns of LB antenna is excited. (a) HPBWs, (b) S paremeter, and (c) radiation patterns.

When the MB and HB DRAs are considered, the frequency band is expected to shift lower and the impedance bandwidths are anticipated to be wider, as shown in the next section. Notably, the radiation patterns of the excited port2 remain stable across the LB as Fig. 7(c) shows. Consequently, the LB antenna utilizing the bandpass FSS Model 1 elements and differential fed to achieve low profile, low coupling, and wideband EM transparency is a promising candidate for TSAA design for the next step.

B. Construction and Operation Mechanism of a Single M/H Band Antenna Element

The design principles for both MB DRAs and HB DRAs are the same. The DRAs were chosen as the antenna element at MB and HB due to their exceptional design flexibility in size, bandwidth, and gain, which can be controlled by the shape and permittivity of the material. Due to high permittivity, the EM waves within the dielectric will be excited with certain modes according to the boundary conditions when the dimensions of the DRAs are determined. The dimensions and permittivity of the DRAs mainly determine the frequency of the exciting mode. Additionally, the specific exciting mode is related to the external excitation, which will directly affect the final radiation pattern of the dielectric resonator (e.g., broadside or conical radiation, etc.). Furthermore, as the operating frequency of the DRAs is inversely proportional to their volume and DRAs have high permittivity, the DRAs can be viewed as a miniaturized antenna, which aligns well with the low-profile requirement of the TSAA array in this study.

The DRAs utilized in this work are based on a double-layer DRA archetype, wherein the bottom layer has a lower permittivity, and the top layer has a higher permittivity. This double-layer DRA design can achieve both wideband and high gain while also requiring a larger volume. In our design, a tri-layer DRA is proposed. By introducing the middle layer into the DRA, the impedance matching, bandwidth, and size can be easily balanced by tuning the air holes' density, height, width, and length.

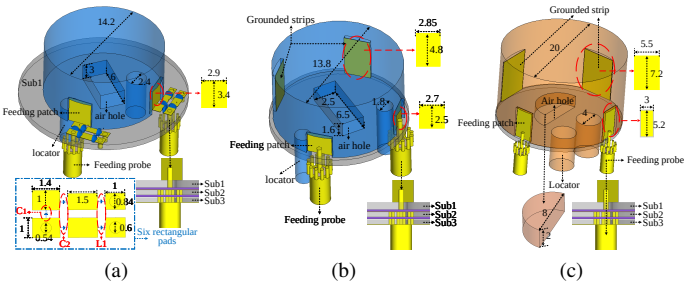

(a) (b) (c)

Fig. 8. Configurations of the proposed HB and MB radiator elements. (a) HB type 1, (b) HB type 2, and (c) MB (units: mm).

1) Construction of the single M/H Band Antenna Element: As shown in Fig. 8, for HB DRAs, two types of three-layer DRAs are used to compensate for the effects of the different positions of HB DRAs in the array. The feeding section of the HB type 1 directly below the LB antenna is equipped with five lumped components (with a capacitor C_1 = 0.7pF, two capacitors C_2 = 1.5pF, and two inductors L_1 = 2.7nH) to improve its coupling with the LB antenna. The introduction of lumped components makes it easier to tune the operating frequency band of the HB type 1 located directly below the LB antenna while maintaining their miniaturization. Six rectangular pads are added to achieve a better impedance match, the outer conductors of the coaxial are grounded, and the inner conductors are attached to the feeding patches on the sidewall of the HB type 1. HB type 2 has two more grounded strips opposite to the feeding patches. Apart from the feeding parts, the overall structure of the HB type 2 located at the four corners below the LB antenna is similar to that of the HB type 1 while the dimensions of the two types are slightly different to maintain HB antennas working at the same frequency band. The bottom layer of the HB DRAs is made of substrate RO4350B with a dielectric constant of 3.66, a loss tangent of 0.0037, and a thickness of 0.764 mm. This substrate layer is the same for all DRAs to simplify fabrication. The middle and top layers are created using 3D printing. The middle layer contains air holes, while the top layer is solid. The 3D printing filament used has a dielectric constant of 11.5 and a loss tangent of 0.0018.

For MB DRAs, all array elements have three layers and are identical, as shown in Fig. 8(c), with the same bottom layer made of RO4350B substrate as the HB DRAs. The middle layer has air holes, and the top layer is solid, which use the same 3D print material as the HB DRAs. The 3-layer structure helps to gain wide bandwidth and improve matching compared with conventional 2-layer DRAs. Two more grounded strips opposite the feeding patches are also embedded to improve the coupling resulting from the LB antennas and HB DRAs.

2) Operation Mechanism of the single M/H Band Antenna Element: As mentioned earlier, the design of DRAs is highly dependent on the dimensions and dielectric properties of the resonator. Since the MB and HB antennas are all DRAs with the same dielectric material and shape, the design principles are comparable. In this paper, the design process of the HB type 2 antenna element of Fig. 9 (a) is used as an example to illustrate. Fig. 9 (a) removes the original floor and decreases the size of the substrate compared with the simulated model to highlight the radiation structures.

Initially, the dimensions of the DRAs are determined based on the desired operating frequency band. In this paper, the HB type2_A antenna element is designed to operate at 5.3-5.7 GHz, as shown in Fig. 9 (b). To enhance the self-cross-polarization couplings of HB type2_A, two additional grounded strips are introduced, opposite to the feeding ports as shown in Fig. 9 (a). The blue line in Fig. 9 (b) indicates that these added strips significantly improve the self-cross-polarization couplings by 17.5 dB at 5.35 GHz. Additionally, the addition of strips allows the working frequency band to shift from 5.55 GHz to a lower frequency 5.34 GHz without increasing the height and diameter of the antenna as shown in the red line of Fig. 9 (b) and the brown line of Fig. 10 (a), which is advantageous for the low-profile design in this paper.

Due to the symmetrical structure of HB DRAs, only simu-

lated results of 1 port of two types working in the free space separately are shown in Fig. 10. HB type 1 and HB type 2 exhibit similar S-parameters over the operating band from 5.1 GHz to 5.6 GHz, with values below -10 dB shown in Fig. 10 (a). it also displays the self-cross-polarization coupling of HB type 1 and HB type 2 separately, which are all less than -15 dB from 5.1 GHz to 5.6 GHz. HB type 2 exhibits lower self-cross-polarization coupling than HB type 1 in the central band, owing to the grounded strips' effects. Fig. 10 (b) depicts the half-power beamwidths and realized gains at different bands for -45 degree polarizations of the two types of HB DRAs. Both HB type 1 and HB type 2 exhibit similar broadside radiation patterns at -45 degree polarization. The realized gains of HB type 1 and HB type 2 are both larger than 5 dBi, and both types of DRAs can achieve a half-power beamwidth larger than 120 degrees over the entire frequency band.

The simulated S-parameters and self-cross-polarization couplings of the MB antenna in Fig. 8 (c) model are as depicted in Fig. 11 (a). The reflection parameters are below -10 dB from 3.3 GHz to 3.55 GHz, and the self-cross-polarization couplings are below -15 dB over the entire frequency band. Fig. 11 (b) shows the half-power beamwidths and realized gains at different bands for the two polarizations. The realized gains are larger than 5.5 dBi for both polarizations, and the half-power beamwidths are larger than 85 degrees over the entire frequency band.

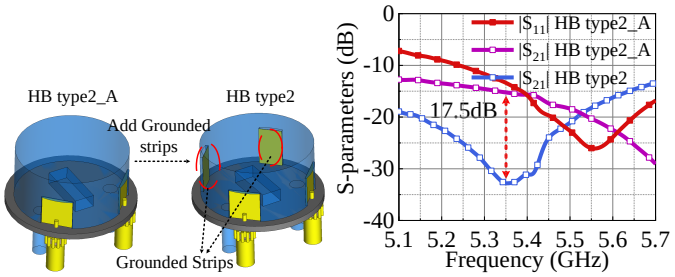

(a) (b)

Fig. 9. S-parameter comparison of HB type 2 element with/without grounded strips. (a) The geometry of HB type 2 with/without grounded strips. (b) S-parameters.

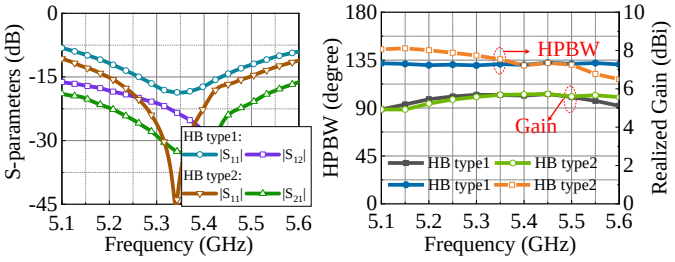

(a) (b)

Fig. 10. Simulated results of proposed HB type 1 and type 2 element. (a) S-Parameters. (b) Realized gains and horizontal HPBWs for -45° polarization.

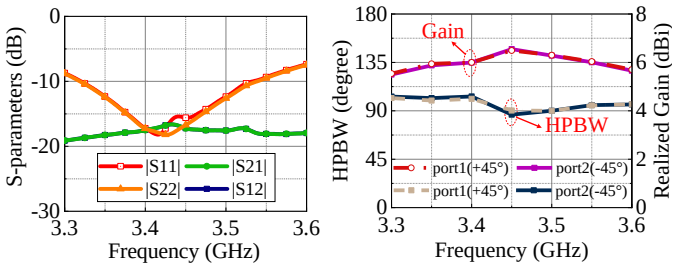

(a) (b)

Fig. 11. Simulated parameters of MB DRA. (a) S-Parameters. (b) Realized gains and horizontal HPBWs.

III. Tri-band Dual-Polarized Shared Aperture Array Performance

In the preceding section, the single antenna elements were analysed separately for each operating band. Fig. 12 depicts the configuration of the sub-array in "Area-1", which is approximately a quarter of the full-scale TSAA. Port numbers L1- and L1+ represent the two polarization ports for the LB patch antenna. The MB DRA ports are represented by M1, M2, M3, M4, and so on, while the HB DRA ports are represented by H1, H2, H3, H4, and so on. In order to meet the conditions for suppressing the grating lobe, two additional MB elements are added between the sub-arrays, such as M3 and M4 shown in Fig. 12 (a). Since the MB antennas between the sub-arrays are less affected by the HB and LB antennas, the ground strip is removed, and the height is lowered compared to the original MB antennas to achieve similar performance. The entire antenna array, consisting of 4 LB antennas, 14 MB DRAs, and 24 HB DRAs, is implemented with a size of 337.5mm x 115mm, as shown in Fig. 12. To provide a better boundary condition to the interested elements, MB and HB antennas with no feed are added on both sides of the full array, as shown in m1, m2, m3, m4, h1, h2, h3, and h4 in Fig. 12. m1, m2, m3, and m4 correspond to the same type as M3, while h1, h2, h3, and h4 correspond to the same type as H1. The impedance matching bandwidth, mutual coupling, and radiation patterns of the LB, MB, and HB antenna arrays of the whole array are simulated and evaluated. Meanwhile, the performance of each frequency band antenna array in the proposed TSAA was compared with that of the TSAA with only one frequency band antenna array, to verify the effectiveness of combining DRAs with FSS in achieving a low profile, decoupling, and restoration of the radiation pattern in multi-band shared aperture antenna array. The structure of the entire array in CST is shown in Fig. 12 (b).

A. Performance of LB Antenna Array of TSAA

Based on the simulated results depicted in Fig. 13 (a), the S-parameters of two dipole antennas of the LB array in two polarizations exhibit over 15 dB isolations between 1.85 GHz and 2.15 GHz. The TSAA also demonstrates a -10 dB impedance bandwidth covering the range from 1.85 GHz to 2.15 GHz. In Fig. 14 (a), the LB antenna of the TSAA array achieves comparable HPBWs and gains as those of the LB

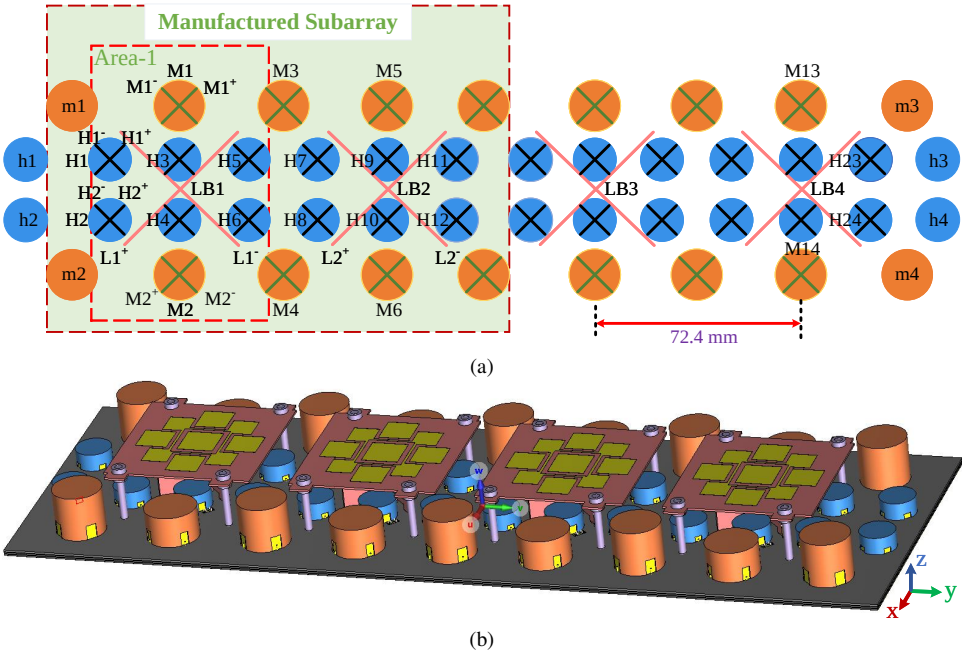

Fig. 12. Configuration of the TSAA. (a) Schematic of the TSAA, and (b) actual simulated model. (LB element separation of 72.4 mm is smaller than the half wavelength of center frequency)

antenna array operating independently. Additionally, Fig. 15 (a) compares the simulated horizontal radiation patterns with and without the DRAs at the HB and MB, demonstrating that the inclusion of DRAs minimally affects the original LB array. Furthermore, the introduction of DRAs at HB and MB effectively mitigates cross-band interference within multi-frequency shared aperture antenna arrays.

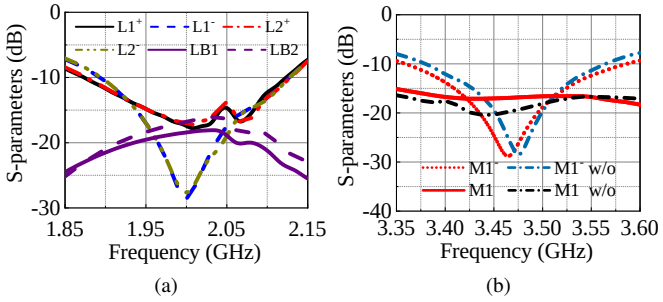

Fig. 13. Simulated S-parameters at different bands. (a) LB ports. (b) MB ports.

B. Performance of MB Antenna Array of TSAA

In this section, the performance of the MB antenna array of TSAA is evaluated for its ability to achieve a low-profile multi-band shared aperture antenna array with reduced cross-band coupling interference. Due to the symmetry of the MB array antenna, only the partially MB elements with relatively poor performance are presented. Fig. 13 (b) presents the simulated S-parameters of M1, which show that the -10 dB impedance bandwidth of M1 ranges from 3.4 GHz to 3.6 GHz. Moreover, the MB antenna array can achieve polarization isolation of less than -15 dB. The introduction of the LB antenna array and the

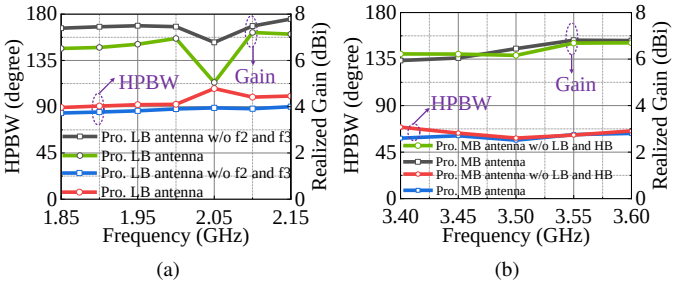

Fig. 14. Simulated HPBWs and gains at different bands. (a) L1- port. (b) M3+ port.

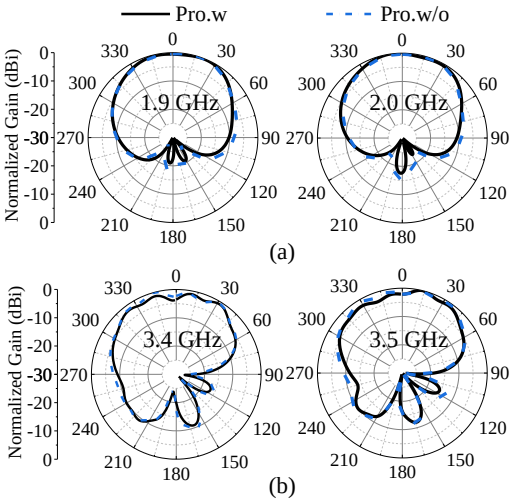

Fig. 15. Comparison of simulated radiation patterns at different bands. (a) Horizontal radiation patterns w and w/o MB and HB when the L1- port is excited. (b) Vertical radiation patterns w and w/o LB and HB when the M3+ port is excited.

HB antenna array has little effect on the working bandwidth and coupling of the MB antenna array. The comparison of simulated HPBWs and gains with and without LB and HB when the M3+ port of the MB antenna array is excited is shown in Fig. 14 (b). It can be observed that the MB antenna array in the TSAA array has similar HPBWs and gains as that of the independent MB array. Furthermore, even when working under the LB antenna with a low profile of 0.13 λ_0, the MB antenna in TSAA can still maintain good antenna performance, with relatively low cross-band coupling interference between the MB antenna and the LB antenna and HB antenna. Therefore, DRAs can be effectively utilized to offset the distorted MB radiation patterns existing in traditional shared aperture antenna arrays, as shown in Fig. 15 (b).

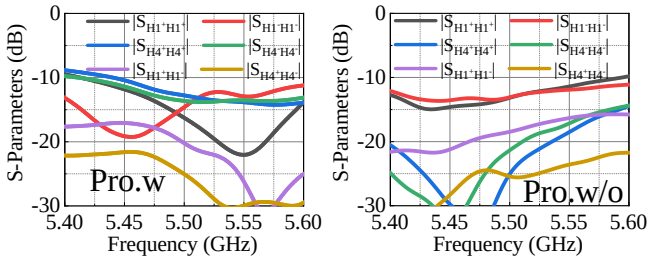

Fig. 16. Simulated S-parameters of the HB antennas located in "Area-1" (a) Proposed HB antennas. (b) Proposed HB antennas without LB and MB antennas.

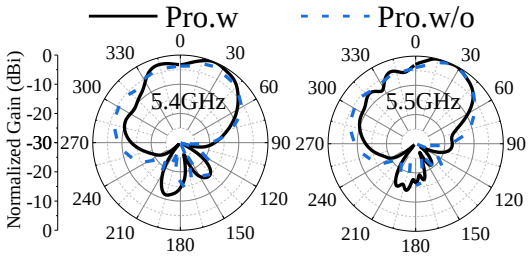

Fig. 17. Comparison of simulated radiation patterns with and without LB and MB when the H1- port of the HB antenna is excited.

C. Performance of HB Antenna Array of TSAA

The HB antenna array is symmetrical, and therefore only the performance of partially "Area-1", composed of H1-H6, is presented in this section. In the absence of decoupling, the VSWR of some HB elements exceed 2, as reported in [8]. However, if DRAs are used instead of dipole antennas, the S-parameters of all HB antennas in the TSAA can be kept below -10 dB from 5.4 GHz to 5.6 GHz, as shown in Fig. 16 (a). Adding the LB and MB arrays has a minor effect on the impedance matching of HB antennas. To observe the distortion of the radiation pattern caused by adding the LB and MB arrays, the H1 antennas with relatively poor performance were selected as examples. the radiation patterns of the conventional HB antenna array will be significantly distorted due to blockage by the LB antennas array and influence from MB antennas array, as reported in [8]. If DRAs are used instead of dipole antennas, the radiation pattern of the HB antenna blocked in the TSAA can keep relatively stable, as shown in Fig. 17.

In addition, the addition of the LB and MB arrays effectively improves the problem of tilted radiation patterns when the HB array is working alone, resulting in a more symmetrical radiation pattern. This improvement is attributed to the adoption of η-shaped stripline coupled feeding technology to excite the LB dipole antenna. Conventional η-shaped stripline coupled fed is typically asymmetric, with the η-shaped stripline located off-center position relative to the radiating patch. This asymmetry can cause inconsistencies in radiation patterns of DRAs operating at middle- and high-frequency bands, as the DRAs located at these bands are situated at two sides of the dipole antennas.

IV. Measured and Simulated Results of the Manufactured Subarray

Due to the large number of MB and HB antennas required in this design, involving 3D printing and numerous manual operations, only half of the TSAA was manufactured and evaluated to optimize time and cost. Due to array symmetry,

Fig. 18. Prototype of the manufactured subarray

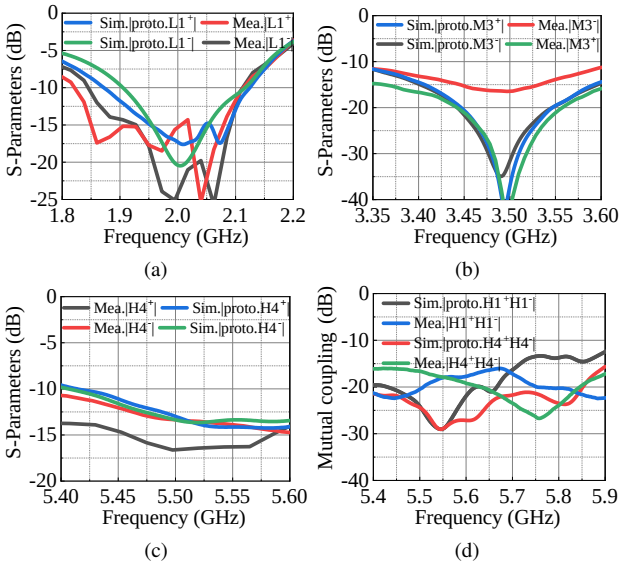

Fig. 19. Comparison of simulated and measured S-parameters for the prototype array.

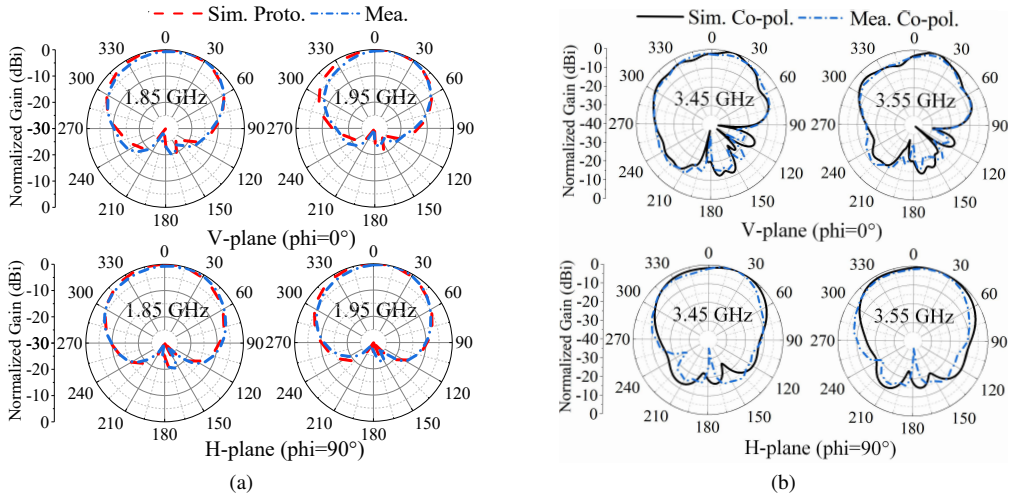

Fig. 20. Simulated and measured radiation patterns for the prototype array. (a) The L2+ port of LB is excited. (b) The M3+ port of MB is excited.

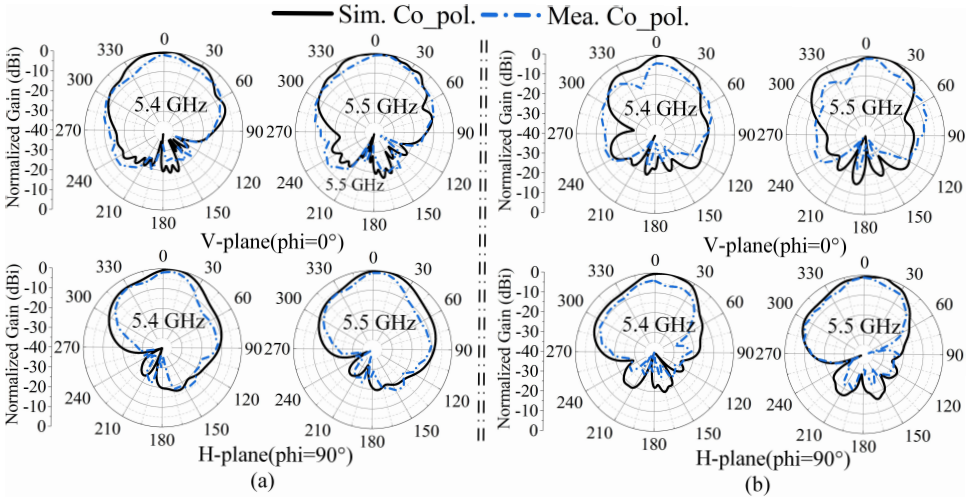

Fig. 21. Simulated and measured radiation patterns of the prototype array when (a) H4+ port and (b) H4- port of HB are excited.

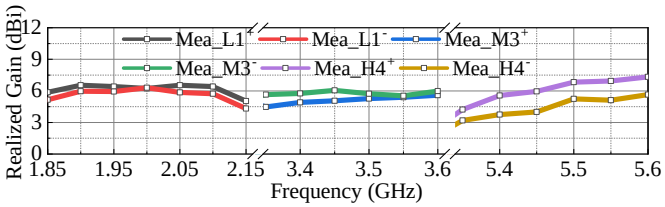

Fig. 22. Measured realized gains of the prototype array when some ports of the LB antenna, the MB antenna and the HB antenna are excited.

the simulated results for both full and half TSAA are nearly identical. This manufactured subarray model, corresponding to the green region in Fig. 12 (a), was denoted as the "prototype array" and was developed to validate the accuracy of the array simulation results, the manufactured prototype is depicted in Fig. 18.

Fig. 19 illustrates a comparison between the simulated and measured S-parameters of the prototype array. The results indicate that almost complete agreement between the simulated and measured S-parameters and the prototype array achieves reflection coefficients of ≤ -10 dB across all operational frequency bands. Furthermore, the prototype array exhibits port-to-port isolation of ≥ 14 dB at HB. Fig. 20 (a) presents the radiation patterns of the prototype array when exciting the L2+ port of LB2. The measured radiation patterns agree well with the simulated ones, and the distortion in the LB pattern, which is common in stacked shared-aperture antennas (as mentioned in [8], [29]), has been effectively restored. Fig. 20 (b) illustrates the radiation patterns of the prototype array when the M3+ port of MB is excited. The measured radiation patterns are similar to the simulated ones, indicating that the interference suffered by MB can be suppressed using the 3D-printing DRAs as MB elements. To save space, the radiation patterns of H4, which is significantly blocked by LB, were selected to validate the simulated results as shown in Fig. 21. The measured HB radiation patterns are in relative agreement with the simulated ones, and the tilted radiation patterns of the HB antenna have been improved. Fig. 22 presents the

measured realized gains of the prototype array, showing stable measured gains at LB. When the ports of MB are excited, the prototype array achieves a measured realized gain of 6 ± 0.5 dBi. Additionally, a measured gain of 6.2 ± 0.8 dBi has been attained in HB.

V. Beam-Steering Property

Wide-angle scanning is the vital function of 5G MIMO antennas. According to several studies [8], [11], [20], using traditional dipoles or patch antennas in a multi-band shared aperture antenna array can result in severe coupling, leading to distorted radiation patterns and poor antenna performance. Despite the introduction of decoupling techniques, the spacing of each frequency band in the multi-band shared aperture antenna array cannot satisfy the condition of being less than 0.7 wavelength, which is necessary to suppress grating lobes during beam scanning. The analysis conducted in the preceding sections affirms that the proposed TSAA satisfies the requirements for achieving wide-angle scanning performance. Specifically, the spacing between adjacent HB, MB, and LB antenna elements meets the conditions necessary to effectively suppress grating lobes. In this section, we employed CST, to further validate the aforementioned conclusion. It should be noted that the whole antenna array only performs beam scanning along the y-direction. The antenna elements in the x-direction are in-phase to increase the gain of the antenna arrays in both MB and HB.

The element spacing of the LB array is 0.48 λ_0 (λ_0 is the free-space wavelength at central frequency of LB). The radiation patterns of the four dipole antennas are simulated with different phase gradients imposed on the dipole antennas. Therefore, at 1.9 GHz, the broadside radiation beam can be obtained when the phases of the LB antenna are the same, while a 168-degree progressive phase gradient is imposed on the LB antennas to achieve a scanning beam of 55 degrees, as can be seen from Fig. 23. For the two polarizations, the array exhibits a large scanning coverage in the yoz plane, and its 3 dB beam coverage can reach ±55 degrees.

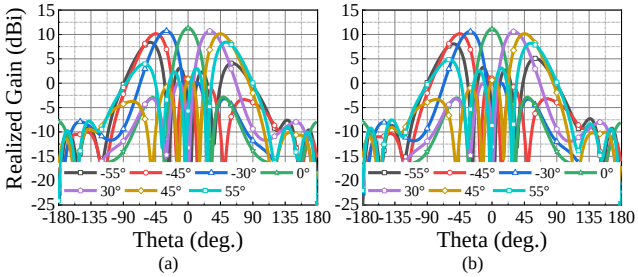

Fig. 23. Simulated LB scanning radiation pattern of the TSAA at 1.9 GHz in yoz plane. (a) -45° polarization. (b) +45° polarization.

The radiation patterns of the DRAs array at MB are simulated and presented when different phase gradients are imposed on DRAs. As shown in Fig. 24 (a) and (c), at 3.4 GHz, the gains of the DRA array are both 13.8 dBi when the radiation beams are at the broadside directions in the two orthogonal polarizations, while the gains of the DRA array are both 10.8 dBi in the two orthogonal polarizations when the radiation beams are scanned to 64 degrees. Also, at 3.5 GHz, the antenna can be scanned to ±60° with a gain roll-off of 3dB, as shown in Fig. 24 (b) and (d).

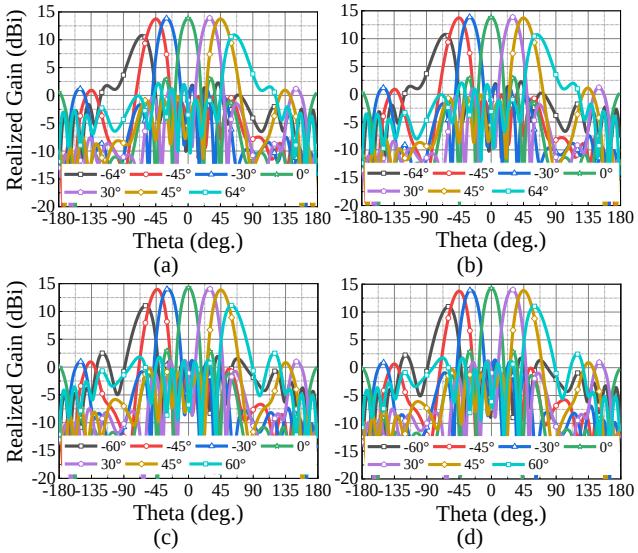

Fig. 24. Simulated MB scanning radiation pattern of the TSAA at different frequencies in yoz plane. -45° polarization: (a) 3.4 GHz; and (c) 3.5 GHz. +45° polarization: (b) 3.4 GHz; and (d) 3.5 GHz.

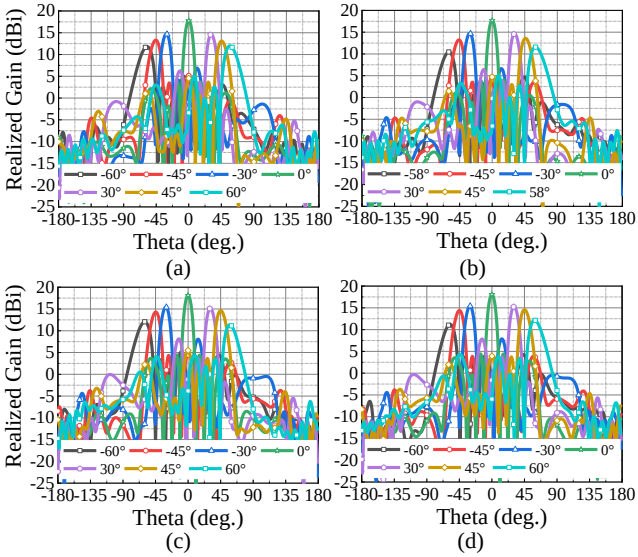

Fig. 25. Simulated HB scanning radiation pattern of the TSAA at different frequencies in yoz plane. -45° polarization: (a) 5.4 GHz; and (c) 5.5 GHz. +45° polarization: (b) 5.4 GHz; and (d) 5.5 GHz.

The DRAs array at HB were simulated to determine its radiation patterns under different phase gradients imposed on DRAs. To achieve a scanning beam of 60 degrees, a 140-degree progressive phase gradient is imposed on HB DRAs. The results presented in Fig. 25 show that at 5.4 GHz, the gains of the DRAs array are 17.8 dBi and 17.7 dBi when

TABLE I: Comparisons of the Proposed and Reported Antennas

Ref.	Operating Frequency (GHz)	Bandwidth	Height (λ_L)	Frequency Ratio	Element Spacing	Scanning Range
[8]	0.79-0.96 & 1.71-2.17 & 3.4-3.6	19.4% & 23.7% & 5.7%	0.242	4:2.22:1	\ & $1.11\lambda_M$ & $0.64\lambda_H$	\ & \ & $\pm60^\circ$
[11]	1.7-2.7 & 3.3-3.6 & 4.8-5	45% & 8.7% & 4%	0.31	2.23:1.56:1	$0.853\lambda_L$ & $0.67\lambda_M$ & $0.95\lambda_H$	\ & \ & \
[20]	0.69-0.96 & 3.5-4.9	32.9% & 33.3%	0.76	5:1	\ & $0.95\lambda_H$	\ & \
[29]	1.8-2.7 & 3.3-3.8	40% & 14.1%	0.192	1.58:1	$0.94\lambda_L$ & $0.74\lambda_H$	\ & \
This work	1.85-2.15 & 3.4-3.6 & 5.4-5.6	15% & 5.7% & 3.6%	0.13	2.75:1.75:1	$0.48\lambda_L$ & $0.42\lambda_M$ & $0.44\lambda_H$	$\pm55^\circ$ & $\pm64^\circ$ & $\pm60^\circ$

the radiation beams are at the broadside directions in the two orthogonal polarizations, respectively. However, the gains of the DRAs array decrease to 12 dBi and 11.6 dBi, respectively, when the radiation beams are scanned to 60 degrees. The gain roll-offs of the DRAs array at 5.4 GHz in the two orthogonal polarizations are 5.8 dB and 6.1 dB, respectively. At 5.5 GHz, the gains of the DRAs array are all 18.1 dBi when the radiation beams are at the broadside directions in the two orthogonal polarizations, while the gains of the DRAs array decrease to 12.1 dBi and 12 dBi, respectively, when the radiation beams are scanned to 58 degrees and 60 degrees. The gain roll-offs of the DRAs array at 5.5 GHz in the two orthogonal polarizations are 6 dB and 6.1 dB, respectively. The radiation patterns of the DRAs array at HB show good beam steering performance. The antenna can steer the beam in a wide range with reasonable gain levels and acceptable gain roll-offs. Detailed comparisons between other shared-aperture antennas and this work are presented in Table I. As can be seen, the wide-angle scanning performance and low profile of the proposed shared-aperture antenna array are much better than the other works.

VI. Conclusion

This study proposes a novel TSAA that employs a deep "Fully-Shared" topology scheme to meet the new requirements of base station antennas for multi-band antenna fusion and independent control. To achieve this, different types of antennas were selected for different operating bands, including an LB antenna with a low profile and a wideband FSS, and 3D-printed DRAs for the MB and HB antennas. The radiation of the HB antenna and MB antenna can, therefore, simultaneously transmit through the LB antenna without being shielded, resulting in an overall low profile, miniaturization, high degree of freedom, and low coupling. The resulting array profile was 0.13 wavelength, and the array element spacing for each frequency band met the scanning conditions for suppressing grating lobes, enabling the large angle of individual control of each frequency band. Furthermore, the study adopted η-shaped stripline coupled feeding technology in the LB antenna to effectively improve tilted radiation patterns of the HB antenna.

Compared to traditional decoupling strategies of shared aperture antenna, the proposed TSAA overcomes their shortcomings, such as the difficulty of expanding the scale of the HB array antenna and the inability to independently control wide-angle scanning for each frequency band. This approach demonstrates the potential for guiding the design of wide-angle scanning TSAA in the future.

References

[1] B. Wang, C. Liao, and C.-H. Du, "A low-profile broadband dual-polarized base station antenna array with well-suppressed cross-polarization," *IEEE Trans. Antennas Propag.*, vol. 69, no. 12, pp. 8354–8365, 2021.

[2] Y. Zhu, Y. Chen, and S. Yang, "Decoupling and low-profile design of dual-band dual-polarized base station antennas using frequency-selective surface," *IEEE Trans. Antennas Propag.*, vol. 67, no. 8, pp. 5272–5281, 2019.

[3] Y. Cui, R. Li, and P. Wang, "Novel dual-broadband planar antenna and its array for 2g/3g/lte base stations," *IEEE Trans. Antennas Propag.*, vol. 61, no. 3, pp. 1132–1139, 2013.

[4] Y. He, Y. Yue, L. Zhang, and Z. N. Chen, "A dual-broadband dual-polarized directional antenna for all-spectrum access base station applications," *IEEE Trans. Antennas Propag.*, vol. 69, no. 4, pp. 1874–1884, 2021.

[5] Y. He, Z. Pan, X. Cheng, Y. He, J. Qiao, and M. M. Tentzeris, "A novel dual-band, dual-polarized, miniaturized and low-profile base station antenna," *IEEE Trans. Antennas Propag.*, vol. 63, no. 12, pp. 5399–5408, 2015.

[6] C.-X. Mao, S. Gao, Q. Luo, T. Rommel, and Q.-X. Chu, "Low-cost x/ku/ka-band dual-polarized array with shared aperture," *IEEE Trans. Antennas Propag.*, vol. 65, no. 7, pp. 3520–3527, 2017.

[7] K. Li, T. Dong, and Z. Xia, "A broadband shared-aperture l/s/x-band dual-polarized antenna for sar applications," *IEEE Access*, vol. 7, pp. 51 417–51 425, 2019.

[8] Y.-L. Chang and Q.-X. Chu, "Suppression of cross-band coupling interference in tri-band shared-aperture base station antenna," *IEEE Trans. Antennas Propag.*, vol. 70, no. 6, pp. 4200–4214, 2022.

[9] W. X. An, H. Wong, K. L. Lau, S. F. Li, and Q. Xue, "Design of broadband dual-band dipole for base station antenna," *IEEE Trans. Antennas Propag.*, vol. 60, no. 3, pp. 1592–1595, 2012.

[10] Z. Wang, G.-x. Zhang, Y. Yin, and J. Wu, "Design of a dual-band high-gain antenna array for wlan and wimax

base station," *IEEE Antennas Wireless Propag. Lett.*, vol. 13, pp. 1721–1724, 2014.

[11] G.-N. Zhou, B.-H. Sun, Q.-Y. Liang, S.-T. Wu, Y.-H. Yang, and Y.-M. Cai, "Triband dual-polarized shared-aperture antenna for 2g/3g/4g/5g base station applications," *IEEE Trans. Antennas Propag.*, vol. 69, no. 1, pp. 97–108, Jan 2021.

[12] L. Zhao, K.-W. Qian, and K.-L. Wu, "A cascaded coupled resonator decoupling network for mitigating interference between two radios in adjacent frequency bands," *IEEE Trans. Microw. Theory Techn.*, vol. 62, no. 11, pp. 2680–2688, 2014.

[13] H. M. Bernety and A. B. Yakovlev, "Reduction of mutual coupling between neighboring strip dipole antennas using confocal elliptical metasurface cloaks," *IEEE Trans. Antennas Propag.*, vol. 63, no. 4, pp. 1554–1563, 2015.

[14] Y. Zhang, X. Y. Zhang, L.-H. Ye, and Y.-M. Pan, "Dual-band base station array using filtering antenna elements for mutual coupling suppression," *IEEE Trans. Antennas Propag.*, vol. 64, no. 8, pp. 3423–3430, 2016.

[15] X.-Y. Zhang, D. Xue, L.-H. Ye, Y.-M. Pan, and Y. Zhang, "Compact dual-band dual-polarized interleaved two-beam array with stable radiation pattern based on filtering elements," *IEEE Trans. Antennas Propag.*, vol. 65, no. 9, pp. 4566–4575, 2017.

[16] H. Huang, X. Li, and Y. Liu, "A novel vector synthetic dipole antenna and its common aperture array," *IEEE Trans. Antennas Propag.*, vol. 66, no. 6, pp. 3183–3188, 2018.

[17] W. Duan, Y. F. Cao, Y.-M. Pan, Z. X. Chen, and X. Y. Zhang, "Compact dual-band dual-polarized base-station antenna array with a small frequency ratio using filtering elements," *IEEE Access*, vol. 7, pp. 127 800–127 808, 2019.

[18] F. Jia, S. Liao, and Q. Xue, "A dual-band dual-polarized antenna array arrangement and its application for base station antennas," *IEEE Antennas Wireless Propag. Lett.*, vol. 19, no. 6, pp. 972–976, 2020.

[19] S. J. Yang and X. Y. Zhang, "Frequency selective surface-based dual-band dual-polarized high-gain antenna," *IEEE Trans. Antennas Propag.*, vol. 70, no. 3, pp. 1663–1671, 2022.

[20] Y. Chen, J. Zhao, and S. Yang, "A novel stacked antenna configuration and its applications in dual-band shared-aperture base station antenna array designs," *IEEE Trans. Antennas Propag.*, vol. 67, no. 12, pp. 7234–7241, 2019.

[21] Y. Zhu, Y. Chen, and S. Yang, "Helical torsion coaxial cable for dual-band shared-aperture antenna array decoupling," *IEEE Trans. Antennas Propag.*, vol. 68, no. 8, pp. 6128–6135, 2020.

[22] T. Li and Z. N. Chen, "Metasurface-based shared-aperture 5g *S* -/ *K* -band antenna using characteristic mode analysis," *IEEE Trans. Antennas Propag.*, vol. 66, no. 12, pp. 6742–6750, 2018.

[23] Y. Zhu, Y. Chen, and S. Yang, "Integration of 5g rectangular mimo antenna array and gsm antenna for dual-band base station applications," *IEEE Access*, vol. 8, pp. 63 175–63 187, 2020.

[24] Y. Cui, X. Gao, H. Fu, Q.-X. Chu, and R. Li, "Broadband dual-polarized dual-dipole planar antennas: Analysis, design, and application for base stations," *IEEE Antennas Propag. Mag.,*, vol. 59, no. 6, pp. 77–87, 2017.

[25] Q. Wu, W. Su, Z. Li, and D. Su, "Reduction in out-of-band antenna coupling using characteristic mode analysis," *IEEE Trans. Antennas Propag.*, vol. 64, no. 7, pp. 2732–2742, 2016.

[26] H. Sheng and Z. N. Chen, "Radiation pattern improvement of cross-band dipoles using inductive-loading mode-suppression method," *IEEE Trans. Antennas Propag.*, vol. 67, no. 5, pp. 3467–3471, 2019.

[27] H.-H. Sun, C. Ding, H. Zhu, B. Jones, and Y. J. Guo, "Suppression of cross-band scattering in multiband antenna arrays," *IEEE Trans. Antennas Propag.*, vol. 67, no. 4, pp. 2379–2389, 2019.

[28] J. C. Soric, A. Monti, A. Toscano, F. Bilotti, and A. Alù, "Dual-polarized reduction of dipole antenna blockage using mantle cloaks," *IEEE Trans. Antennas Propag.*, vol. 63, no. 11, pp. 4827–4834, 2015.

[29] D. He, Q. Yu, Y. Chen, and S. Yang, "Dual-band shared-aperture base station antenna array with electromagnetic transparent antenna elements," *IEEE Trans. Antennas Propag.*, vol. 69, no. 9, pp. 5596–5606, 2021.